

A Framework for Fully Programmable Frequency-Encoded Quantum Networks Harnessing Multioutput Quantum Pulse Gates

Patrick Folge[✉], * Michael Stefszky[✉], Benjamin Brecht, and Christine Silberhorn

*Integrated Quantum Optics, Institute for Photonic Quantum Systems (PhoQS), Paderborn University,
Warburgerstr. 100, Paderborn 33098, Germany*



(Received 9 February 2024; revised 31 May 2024; accepted 22 October 2024; published 26 November 2024)

Linear optical quantum networks, consisting of a quantum input state and a multiport interferometer, are an important building block for many quantum technological concepts, e.g., Gaussian boson sampling. Here, we propose the implementation of such networks based on frequency conversion by utilizing a so-called multioutput quantum pulse gate (MQPG). This approach allows the resource-efficient and therefore scalable implementation of frequency-bin-based, fully programmable interferometers in a single spatial and polarization mode. Quantum input states for this network can be provided by utilizing the strong frequency entanglement of a type-0 parametric down-conversion (PDC) source. Here, we develop a theoretical framework to describe linear networks based on an MQPG and PDC and utilize it to investigate the limits and scalability of our approach.

DOI: [10.1103/PRXQuantum.5.040329](https://doi.org/10.1103/PRXQuantum.5.040329)

I. INTRODUCTION

Linear optical quantum networks (LOQNs), which we consider as a multiport interferometer with a quantum input state and followed by photon counting or homodyne detection, have become an increasingly relevant platform and building block for many quantum technological applications. These include (Gaussian) boson sampling [1–3], measurement-based quantum computation [4,5], quantum teleportation [6,7], quantum walks [8–10], and quantum simulations [11,12]. However, to enable useful applications of these concepts, which extend beyond proof-of-principle demonstrations, the underlying LOQNs have to reach sufficiently high dimensionality in terms of both contributing modes and photons. Recent implementations of high-dimensional LOQNs were achieved in both the spatial [13] and temporal [14] degrees of freedom and were able to prove quantum computational advantages. However, these approaches require many optical components as well as synchronization and phase-stable implementation of large experimental setups. Thus, scaling these approaches is a challenging technical task.

LOQNs can also be implemented using spectral encodings and have been explored by using electro-optical modulators (EOMs) [15–20] or spectrally multimode

homodyne detection [21–23]. However, the EOM-based approach requires active spectral shaping of the input quantum state that can result in significant losses and the implementation of arbitrary LOQNs requires complex pulse shapes of the electrical radio-frequency signals. On the other hand, the homodyne-based approach faces the challenge of introducing non-Gaussian elements, which are a crucial requirement for many of the above-mentioned applications, and require a phase-stable implementation.

In this paper we explore an alternative approach for LOQNs in the spectral domain that is based on frequency conversion. This introduces a new platform for photonic quantum information processing and offers a highly efficient implementation of intrinsically phase-stable quantum networks with full programmability. The general concept of an LOQN is depicted in Fig. 1 and illustrates the main requirements: controlled preparation of input quantum states, a stable but reconfigurable multiport interferometer, and detection. At the core of our approach lies a multioutput quantum pulse gate [24], allowing one to implement a fully programmable frequency-bin interferometer [25]. In combination with a highly multimode type-0 parametric down-conversion (PDC) source, one can realize a high-dimensional LOQN in one spatial mode by using only two nonlinear waveguides. Note that if used together with detection in the photon-number basis, our scheme does not require active phase stabilization.

This work is organized as follows. First, we introduce the theoretical modeling of the MQPG, and discuss how it can be utilized to implement interferometers based on frequency bins. Next, we introduce type-0 PDC as an appropriate source of input quantum states for the LOQN

*Contact author: patrick.folge@upb.de

Published by the American Physical Society under the terms of the [Creative Commons Attribution 4.0 International](https://creativecommons.org/licenses/by/4.0/) license. Further distribution of this work must maintain attribution to the author(s) and the published article's title, journal citation, and DOI.

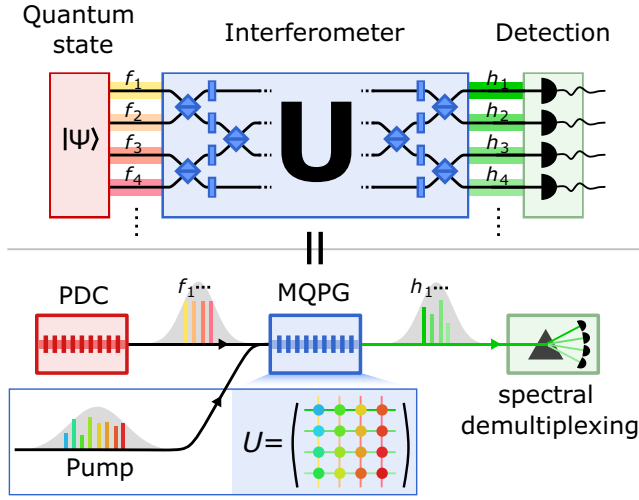


FIG. 1. Top: schematic depiction of an LOQN. The multiport interferometer is characterized by a unitary matrix U , describing how input and output modes are connected. A quantum state is used as the quantum resource of the system. Bottom: our scheme to implement such an LOQN in a spectral encoding. The quantum state, provided by a type-0 PDC source, is interfered in an MQPG that acts as the interferometer and is fully reconfigurable via its pump.

and theoretically model the combined system of PDC and MQPG. For this, we derive a formalism that allows us to investigate the quality of the frequency conversion-based LOQN via the squeezing strength and purity of the output state. As an instructive example, we apply our framework to simulate a minimal example of an LOQN composed of a frequency-bin beam splitter and squeezed input states. Finally, we investigate the fundamental limits of our scheme and explore its scalability to higher numbers of contributing modes.

II. THEORETICAL MODEL

In this work, we assume that all fields are in the form of optical pulses, which are described by a complex spectral amplitude $F(\omega)$. Such modes are usually labeled temporal modes (TMs) [26]. Furthermore, we assume for simplicity that all fields are in one spatial and polarization mode. The creation operator of a photon in such a TM is given by [26,27]

$$\hat{F}^\dagger = \int d\omega F^*(\omega) \hat{a}^\dagger(\omega). \quad (1)$$

We label operators associated with TM $F(\omega)$ with the same capital letter and a hat, i.e., \hat{F} .

A. Frequency-bin interferometer

At the heart of a general LOQN lies a multiport interferometer, preferably programmable, which allows one to

interfere and process the input states. Such an interferometer (e.g., based on spatial modes) is characterized by a unitary matrix U_{kl} , which describes how the (spatial) input modes \hat{f}_l are connected to the (spatial) output modes \hat{h}_k via the operator transformation

$$\hat{h}_k = \sum_{l=1}^{N_{\text{in}}} U_{kl} \hat{f}_l. \quad (2)$$

Here, N_{in} is the number of input modes and therefore also the dimension of the unitary matrix. In other words, Eq. (2) implies that the interferometer's outputs correspond to different superpositions of the inputs, while maintaining energy conservation.

In this work, we present a scheme to implement such an interferometer on the basis of a set of N_{in} -separated frequency bins $A_l(\omega_{\text{in}})$, where l labels the individual bins at central frequency $\bar{\omega}_l^{\text{in}}$ and the ω_{in} dependence encodes the spectral profile of the bins (e.g., Gaussian). We first define a set of superposition modes

$$S_k(\omega_{\text{in}}) := \sum_{l=1}^{N_{\text{in}}} U_{kl} A_l(\omega_{\text{in}}), \quad (3)$$

which correspond to the outputs of the interferometer. The mode operators of these then take the form $\hat{S}_k = \sum_{l=1}^{N_{\text{in}}} U_{kl} \hat{A}_l$ and contain operators \hat{A}_l pertaining to the individual bins. To implement an interferometer on the frequency-bin basis, we now design a process that is capable of operating on the superposition modes \hat{S}_k given by Eq. (3). In the following we present the details for an experimental implementation of this task, which utilizes a so-called multioutput quantum pulse gate (MQPG).

B. The MQPG as an interferometer

An MQPG is a specially designed sum-frequency generation (SFG) process in a periodically poled nonlinear waveguide [24,28]. As an SFG process, it is characterized by a transfer function (TF)

$$G_{\text{SFG}}(\omega_{\text{in}}, \omega_{\text{out}}) = P(\omega_P = \omega_{\text{out}} - \omega_{\text{in}}) \Phi(\omega_{\text{in}}, \omega_{\text{out}}), \quad (4)$$

which is the product of the phase-matching function $\Phi(\omega_{\text{in}}, \omega_{\text{out}})$ of the nonlinear process and the complex spectrum $P(\omega_P)$ of the pump [29]. This TF describes how the amplitudes at input frequencies ω_{in} are converted to the output frequencies ω_{out} . The distinct property of an MQPG, setting it apart from general SFG, is group velocity matching of the pump and signal fields, which can be achieved by dispersion engineering of the waveguides [28]. Because of this, the PM function of an MQPG is oriented perpendicular to the output axis, which leads to a situation where

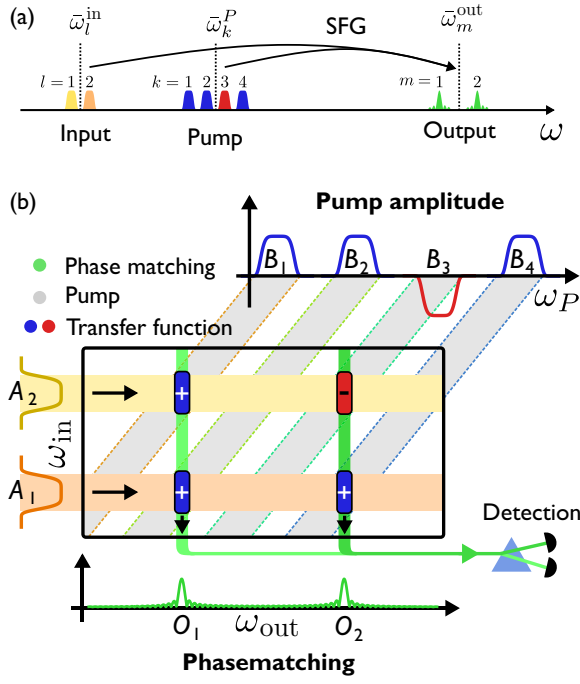


FIG. 2. (a) A depiction of the contributing frequency ranges in the MQPG process. (b) Schematic depiction of the transfer function G of a two-output MQPG, implementing a frequency-bin beam splitter, which connects two input bins (A_l) to two output modes (O_m). The transfer function (red and blue) is given as the product of the phase-matching function Φ (green) and the pump spectrum P (gray). Imprinting specific amplitudes and phases onto the pump allows one to program different transfer functions. Here four pump bins (B_k) realize the beam splitter.

the output frequency does not change for a broad input frequency range.

Note that the original quantum pulse gate [28,30] had only one output, but recently the concept has been expanded for multiple outputs, making it ideal for network applications [24]. The MQPG combines multiple spectrally separated phase-matching peaks within one device, by modulating the periodic poling with a superstructure. The PM function of such an MQPG with N_{out} peaks then has the form

$$\Phi(\omega_{\text{in}}, \omega_{\text{out}}) \approx \sum_{m=1}^{N_{\text{out}}} O_m(\omega_{\text{out}}), \quad (5)$$

where $O_m(\omega_{\text{out}})$ describes the peak's spectral profile (typically sinc shape) and m labels the different central positions $\bar{\omega}_m^{\text{out}}$ of the peaks [31]. The PM function of such an MQPG is depicted in Fig. 2, where we sketch the MQPG's general working principle for two inputs and outputs.

The MQPG allows us to perform operations on arbitrarily chosen superposition modes of frequency bins. This works under the assumption that the pump structures [here frequency bins with spectral profile $B(\omega_P)$]

are spectrally broader than the individual phase-matching peaks $O_m(\omega_{\text{out}})$ [32]. Since the MQPG is an SFG process, such a pump bin with a central frequency of $\bar{\omega}^{\text{pump}}$ addresses an input frequency bin with a central frequency of $\bar{\omega}_m^{\text{in}} = \bar{\omega}_m^{\text{out}} - \bar{\omega}^{\text{pump}}$ and converts it to the m th output with a central frequency $\bar{\omega}_m^{\text{out}}$. In more detail this means that conversion is achieved at the intersection of the bins's pump function $B(\omega_P)$ and the PM function; hence, an input bin $A_m(\omega_{\text{in}}) = B(\bar{\omega}_m^{\text{out}} - \omega_{\text{in}})$ is converted to the output mode O_m . Note that this input mode has the same complex spectral profile as the corresponding pump bin, but is frequency shifted. Furthermore, due to the orientation of the PM function, the shape and position of the output modes do not change when the pump bin is shifted. This crucial feature allows for the necessary multipath interference of interferometers, since multiple input modes can be coherently mapped to the same output by utilizing multiple pump bins (see Fig. 2). Since the phase and amplitude of the pump bins also determine the phase and amplitude of the conversion, we can implement the mapping of one of the superposition modes S_k to one of the output modes O_m . This is done by appropriately choosing the pump bins so that all outputs address the same input bins at centers $\bar{\omega}_l^{\text{in}}$. With this, it is possible to realize a multiport interferometer, by programming a pump spectrum of the form

$$P(\omega_P) = \sum_{m=1}^{N_{\text{out}}} \sum_{l=1}^{N_{\text{in}}} U_{ml} B(\bar{\omega}_m^{\text{out}} - \bar{\omega}_l^{\text{in}} - \omega_P). \quad (6)$$

Here, $P(\omega_P)$ is the complete pump spectrum, which is composed of individual frequency bins labeled by the corresponding frequencies of the input and output bins and weighted by the corresponding entry U_{ml} of the unitary matrix describing the network. Using this yields a TF

$$\begin{aligned} G_U(\omega_{\text{in}}, \omega_{\text{out}}) &= \sum_{m=1}^{N_{\text{out}}} \sum_{l=1}^{N_{\text{in}}} U_{ml} A_l(\omega_{\text{in}}) O_m(\omega_{\text{out}}) \\ &= \sum_{m=1}^{N_{\text{out}}} S_m(\omega_{\text{in}}) O_m(\omega_{\text{out}}). \end{aligned} \quad (7)$$

One simple example of this scheme is depicted in Fig. 2, namely, the implementation of the TF for a balanced beam splitter $[U_{\text{BS}} = \{(1, 1), (1, -1)\}/\sqrt{2}]$ on the frequency-bin basis. The TF in this case is given by

$$\begin{aligned} G_{\text{BS}}(\omega_{\text{in}}, \omega_{\text{out}}) &= [A_1(\omega_{\text{in}}) + A_2(\omega_{\text{in}})] O_1(\omega_{\text{out}})/\sqrt{2} \\ &\quad + [A_1(\omega_{\text{in}}) - A_2(\omega_{\text{in}})] O_2(\omega_{\text{out}})/\sqrt{2}. \end{aligned} \quad (8)$$

To understand the action of such an MQPG on a quantum input state, we can consider the problem within the Heisenberg picture, where a general SFG process is described via

the Bogoliubov transformations [29]:

$$\hat{b}''(\omega_{\text{in}}) = \int d\omega'_{\text{in}} U_b^{\mathcal{O}}(\omega_{\text{in}}, \omega'_{\text{in}}) \hat{b}'(\omega'_{\text{in}}) + \int d\omega'_{\text{out}} V_b^{\mathcal{O}}(\omega_{\text{in}}, \omega'_{\text{out}}) \hat{a}'(\omega'_{\text{out}}), \quad (9)$$

$$\hat{a}''(\omega_{\text{out}}) = \int d\omega'_{\text{out}} U_a^{\mathcal{O}}(\omega_{\text{out}}, \omega'_{\text{out}}) \hat{a}'(\omega'_{\text{out}}) - \int d\omega'_{\text{in}} V_a^{\mathcal{O}}(\omega_{\text{out}}, \omega'_{\text{in}}) \hat{b}'(\omega'_{\text{in}}). \quad (10)$$

Here, the operators representing the fields in front of the SFG are labeled with single-prime notation and fields after the SFG with double-prime notation [see Fig. 3(a)]. We consider two different monochromatic operators \hat{a} and \hat{b} for input and output modes to account for the possibility of having orthogonal polarizations and for the two separated frequency ranges of ω_{in} and ω_{out} . Functions $U_a^{\mathcal{O}}, V_a^{\mathcal{O}}, U_b^{\mathcal{O}}, V_b^{\mathcal{O}}$ can be calculated directly from the TF, when time-ordering effects [29,33] are neglected (see Appendix D). Equation (10) for an MQPG with TF (7) simplifies to

$$\hat{S}_m'' = \cos(\theta_m) \hat{S}_m' + \sin(\theta_m) \hat{O}_m', \quad (11a)$$

$$\hat{O}_m'' = \cos(\theta_m) \hat{O}_m' - \sin(\theta_m) \hat{S}_m'. \quad (11b)$$

These are the Heisenberg operator transformations for the superposition modes of the MQPG. Parameter θ_m defines the conversion efficiency $\sin(\theta_m)^2$ of the m th mode. It can be adjusted with the pump power and can in principle reach unity [34]. In this case ($\theta_m = \pi/2$) Eq. (11) takes the form

$$\hat{O}_m'' = -\hat{S}_m' = -\sum_{l=1}^{N_{\text{in}}} U_{ml} \hat{A}_l', \quad (12)$$

which is equivalent to relation (2), characterizing the multiport interferometer. Note however that Eq. (12) is formulated in terms of frequency bins that are connected via frequency conversion.

The action of an MQPG can also be interpreted as a coherent filtering of a superposition mode S_m and the simultaneous quantum transduction to an output mode O_m . We call this process coherent filtering, because it is sensitive to the spectral phase of the considered modes. In the next section, we describe a source of input states that are naturally compatible with the MQPG.

C. Spectrally multimode squeezing source

One desirable set of input states for LOQNs are squeezed states, for example in Gaussian boson sampling, which we consider here. An optimal source for

our frequency-bin-based network would deliver squeezed states in the input bins $A_k(\omega_{\text{in}})$. However, such sources are challenging to engineer and would require a sophisticated control of the PDC process, e.g., by utilizing resonators [35]. Therefore, we consider the use of well-established degenerate type-0 PDC sources, which in the high-gain regime generate squeezed states in many TMs [21,36]. Such PDC sources are characterized by their joint spectral amplitude (JSA)

$$f(\omega_{\text{in}}, \omega'_{\text{in}}) = P(\omega_P = \omega_{\text{in}} + \omega'_{\text{in}}) \Phi(\omega_{\text{in}}, \omega'_{\text{in}}), \quad (13)$$

which is given as the product of the pump amplitude spectrum and phase-matching function [37]. Note that, since the signal and idler are indistinguishable in type-0 PDC, the JSA has to fulfill $f(\omega_{\text{in}}, \omega'_{\text{in}}) = f(\omega'_{\text{in}}, \omega_{\text{in}})$. The evolution of an input state (here vacuum) passing through the PDC is given by the unitary operator

$$\hat{U}_{\text{PDC}} = \exp \left(-\frac{i}{\hbar} \int d\omega_{\text{in}} d\omega'_{\text{in}} f(\omega_{\text{in}}, \omega'_{\text{in}}) \times \hat{b}^\dagger(\omega_{\text{in}}) \hat{b}^\dagger(\omega'_{\text{in}}) + \text{H.c.} \right). \quad (14)$$

For a type-0 PDC source, the JSA is given as a narrow stripe oriented along the antidiagonal [as illustrated in Fig. 3(b)]. This results from the orientation of the pump function P and the phase matching ϕ along this axis [38]. Note that this allows one to filter out sinc side lobes in the JSA, without the need of apodized poling, simply by appropriately choosing the spectral width of the pump. For a very narrow pump, the JSA can be approximated by a δ function, i.e.,

$$f(\omega_{\text{in}}, \omega'_{\text{in}}) \propto \delta(\omega_{\text{in}} + \omega'_{\text{in}} - 2\omega_0) \propto \sum_k \phi_k(\omega_{\text{in}} - \omega_0) \phi_k^*[-(\omega'_{\text{in}} - \omega_0)], \quad (15)$$

which can be decomposed into any orthonormal basis $\{\phi_k\}$ fulfilling the completeness relation $\delta(\omega - \omega') = \sum_k \phi_k(\omega) \phi_k^*(\omega')$. Note that in Eq. (15) the paired functions are mirrored around the degeneracy point ω_0 , e.g., a bin A_1 at a central frequency $\omega_0 + \Delta$ is paired with a bin A_2 centered at $\omega_0 - \Delta$. Since these bins are part of an orthonormal basis, unitary (14) takes on the form $\hat{U}_{\text{PDC}} = \hat{U}_{12} \otimes \hat{U}_{\text{rest}}$, where the unitary describing the subspace of the bins is

$$\hat{U}_{12} = \exp(\alpha \hat{A}_1^\dagger \hat{A}_2^\dagger - \alpha^* \hat{A}_1 \hat{A}_2) \quad (16)$$

and is independent of unitary \hat{U}_{rest} that describes the remaining space. Note that Eq. (16) has the form of the well-known two-mode squeezing operator [39]. This shows that such a PDC source provides two-mode

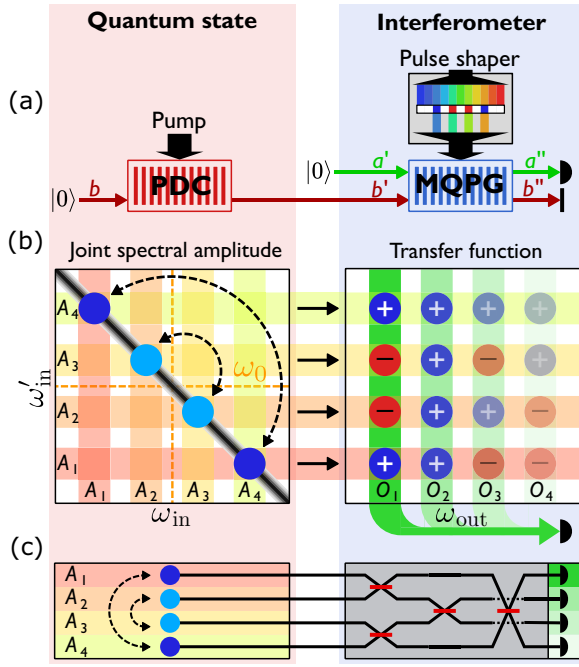


FIG. 3. (a) Schematic depiction of the combined system of the type-0 PDC source and MQPG. The transfer function of the MQPG can be programmed to implement an arbitrary interferometer by shaping the pump. (b) Left: schematic depiction of the JSA in black. The blue areas highlight the effective JSA that is coherently filtered from the PDC state by the MQPG. The dashed arrows highlight different two-mode squeezed states. Right: the transfer function of the MQPG that maps the coherently filtered bins into different superpositions to different output channels. (c) Analogous interferometer in the spatial domain.

squeezed (TMS) states between pairs of frequency bins. Parameter α combines multiple constants, including the pump strength, and determines the squeezing strength.

However, for the physical scenarios envisioned here, the pump linewidth cannot be neglected in the JSA, and the approximation of Eq. (15) no longer applies. Therefore, we consider a general description of type-0 PDC in our model, which allows us to consider any shape of the JSA. This will enable us to study the influences of its non-negligible width in later sections. We model the PDC in the Heisenberg picture where Eq. (14) takes the form of the Bogoliubov transformation

$$\begin{aligned} \hat{b}'(\omega_{\text{in}}) &= \int d\omega'_{\text{in}} U^P(\omega_{\text{in}}, \omega'_{\text{in}}) \hat{b}(\omega'_{\text{in}}) \\ &+ \int d\omega'_{\text{in}} V^P(\omega_{\text{in}}, \omega'_{\text{in}}) \hat{b}^\dagger(\omega'_{\text{in}}). \end{aligned} \quad (17)$$

Here, fields after the PDC are labeled with prime notation, while fields in front of the PDC do not have an additional label [see Fig. 3(a)]. Equation (17) is similar to Eq. (10) of the SFG process; however, only one set of monochromatic operators \hat{b} is considered here, since the signal and

idler fields have the same polarization and central frequency. Functions U^P and V^P can be derived from the JSA (see Appendix C) if time-ordering effects are neglected [29]. This first-order approximation restricts our analysis to moderate squeezing levels around 12 dB [40,41], since, for higher gain, time-ordering effects can alter the generated state. The validity of this approximation is confirmed in Appendix F.

D. Describing the complete LOQN

In summary, our scheme to implement LOQNs reads as follows. A type-0 PDC generates TMS states between pairs of frequency bins, which are subsequently coherently filtered and superimposed in the output modes of an MQPG. The resulting quantum state in the outputs is then analogous to the output state of a spatial interferometer with TMS states in the input. In Fig. 3 we illustrate our proposed scheme for a specific example network. We depict the required experimental components of our specific PDC source and a fully programmable MQPG. To model this combined system, we adapt the theory of intensity filtered type-2 PDC presented in Ref. [42] to include the coherent filtering by the MQPG. This enables us to describe the frequency-converted quantum state ρ_{out} in the MQPG's output in the continuous-variable picture via its covariance matrix σ_{kl} . This is possible since we consider only Gaussian transformations (squeezing and beam splitters) [43,44]. Because of the fact that the MQPG's output only consists of modes O_K , we can describe the full output state on the basis of operators \hat{O}_k . The quadrature operators $\hat{X}_k = (\hat{O}_k + \hat{O}_k^\dagger)/\sqrt{2}$ and $\hat{Y}_k = (\hat{O}_k - \hat{O}_k^\dagger)/i\sqrt{2}$ corresponding to the different output modes can be arranged in the vector

$$\vec{\hat{R}} = (\hat{X}_1, \hat{Y}_1, \hat{X}_2, \hat{Y}_2, \dots). \quad (18)$$

Then the individual elements of the covariance matrix can be expressed as

$$\sigma_{kl} = \frac{1}{2} \langle \hat{R}_k \hat{R}_l + \hat{R}_l \hat{R}_k \rangle - \langle \hat{R}_k \rangle \langle \hat{R}_l \rangle. \quad (19)$$

In the following we neglect the last term because we assume vacuum states in all fields in front of the nonlinear elements. Note however that this is not a necessity and that our framework can be readily adapted to include other input states. We describe the evolution of the states in the Heisenberg picture, by successively applying transformations (10) and (17) to operators \hat{O}'_k , which results in the expression

$$\begin{aligned} \hat{O}'_k &= \int d\omega_{\text{out}} H_k^1(\omega_{\text{out}}) \hat{a}'(\omega_{\text{out}}) \\ &+ \int d\omega_{\text{in}} H_k^2(\omega_{\text{in}}) \hat{b}(\omega_{\text{in}}) + H_k^3(\omega_{\text{in}}) \hat{b}^\dagger(\omega_{\text{in}}), \end{aligned} \quad (20)$$

where the amplitude functions take the form

$$\begin{aligned}
 H_k^1(\omega_{\text{out}}) &= \int d\omega'_{\text{out}} O_k(\omega'_{\text{out}}) U_a^Q(\omega'_{\text{out}}, \omega_{\text{out}}), \\
 H_k^2(\omega_{\text{in}}) &= - \int d\omega'_{\text{out}} d\omega'_{\text{in}} O_k(\omega'_{\text{out}}) V_a^Q(\omega'_{\text{out}}, \omega'_{\text{in}}) \\
 &\quad \times U^P(\omega'_{\text{in}}, \omega_{\text{in}}), \\
 H_k^3(\omega_{\text{in}}) &= - \int d\omega_{\text{out}} d\omega'_{\text{in}} O_k(\omega'_{\text{out}}) V_a^Q(\omega'_{\text{out}}, \omega'_{\text{in}}) \\
 &\quad \times V^P(\omega'_{\text{in}}, \omega_{\text{in}}).
 \end{aligned}$$

Inserting these operators into Eq. (19) then allows one to calculate the covariance matrix for any given JSA and TF, by evaluating the vacuum expectation values. The resulting form of σ_{kl} is derived in Appendix E. We would like to point out that our scheme, despite our description in the framework of continuous-variable quantum optics, does not assume any particular detection method. Experimentally, it is fully compatible with detection in the photon-number basis after separating the different output channels by frequency filtering. While simulating this scenario is computationally demanding since it is effectively a Gaussian boson sampling system, the photon-number distributions can in principle be derived from the covariance matrix [45].

III. FREQUENCY BEAM SPLITTER

As an instructive example of our scheme, we simulate the implementation of a simple LOQN, namely, the interference of both modes from a TMS state on a balanced beam splitter. For this, we expect two independent single-mode squeezed (SMS) states in the output, since this scenario is the reverse of the well-known generation of TMS states by interfering SMS states on a beam splitter [39].

The scenario is depicted in Fig. 4, where we summarize the simulation by displaying the JSA and TF utilized as input for the calculation together with the resulting covariance matrices both after the PDC and at the output of the LOQN. To keep the results as general as possible, we define the spectral dimensions (bin width, positions, etc.) in terms of the simulation's input range $\Delta\omega_{\text{in}}$, which bounds the simulation area. In an experimental setting, this range can be understood as the bandwidth over which our scheme can operate and that is limited, for example, by the limited pump spectrum of the MQPG. To highlight the experimental feasibility of our scheme, we provide simulations of realistically achievable nonlinear processes in periodically poled LiNbO₃ waveguides in Appendix A, according to which we model our idealized simulations presented here. This results in a JSA that is approximated as a Gaussian cross section of width $\text{FWHM}_{\text{JSA}} = 0.05\Delta\omega_{\text{in}}$ oriented along the antidiagonal [see Fig. 4(b)].

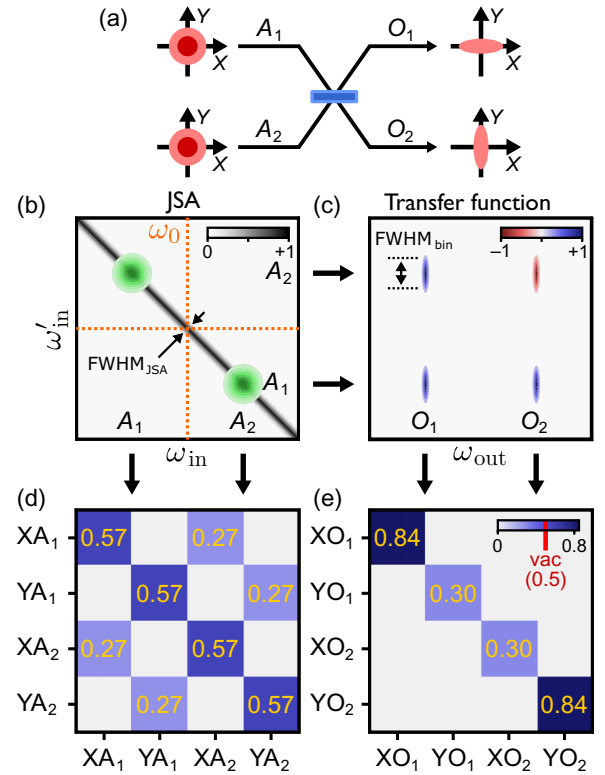


FIG. 4. Simulation of a frequency beam splitter, mapping bins A_1 and A_2 to bins O_1 and O_2 . (a) Analogous spatial domain scenario. (b) Joint spectral amplitude (JSA) of the PDC. Green dots show the perfect two-mode squeezed JSA between bins A_1 and A_2 . (c) Transfer function of the MQPG. (d) Absolute value of the covariance matrix between bins A_1 and A_2 after PDC and (e) between bins O_1 and O_2 after the MQPG.

We normalize this JSA to a mean photon number of $\bar{n} = 1$ within the simulation region, to obtain experimentally realistic squeezing values. The frequency-bin beam splitter on the other hand is modeled by considering a TF of the form (8), where we consider Gaussian shapes for all modes (A_1 , A_2 , O_1 , O_2). The input bins were chosen to have width $\text{FWHM}_{\text{bin}} = 0.1\Delta\omega_{\text{in}}$, larger than FWHM_{JSA} .

First, we only consider the PDC and calculate the covariance matrix between two bins A_1 and A_2 that are placed symmetrically around the degeneracy point at ω_0 . For this, we apply Eq. (17) to the broadband operators \hat{A}_1 and \hat{A}_2 and then evaluate Eq. (19) for the corresponding quadrature operators. As expected from the discussion above, the resulting covariance matrix [see Fig. 4(c)] represents a TMS state. This is evident from the submatrices of the individual modes, which show noise above the vacuum level of 0.5 (as one would expect from a thermal state), while being correlated when considered a joint system.

The covariance matrix between the output modes O_1 and O_2 after the MQPG is derived by applying our theoretical model of the complete LOQN to discretized versions (1500×1500 points) of the JSA and TF. The resulting

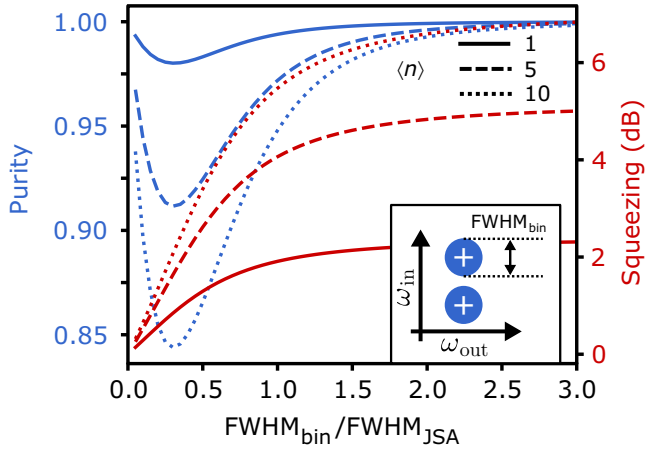


FIG. 5. Squeezing and purity calculated from the covariance matrix after the frequency beam splitter for different input bin widths FWHM_{bin} . The different line types correspond to different normalizations of the JSA, which is proportional to the pump strength.

covariance matrix [depicted in Fig. 4(d)] is showing two independent SMS states, which becomes apparent from the two quadrature variances (diagonal elements) that are squeezed below the vacuum level. As previously discussed, this is the expected result for the interference of a TMS state on a beam splitter and therefore establishes the capability of our scheme to implement the LOQN, even when realist PDC sources with a finite JSA width are considered.

To better understand the limits of our scheme, we explore the quality of the output state for varying widths of the input bins A_k . Here, we only consider the even output ($A_1 + A_2$) of the MQPG. We quantify the quality of the output state by calculating the purity and squeezing strength of this state from the resulting covariance matrix. The purity is given by $\gamma = \text{tr}(\rho_{out}^2) = 1/[2^N \sqrt{\det(\sigma)}]$ [43] and the squeezing strength in decibels as $S = -10 \log_{10}(2a)$, where a is the minimal eigenvalue of σ [46]. We simulate these quantities for input bins in a range from $\text{FWHM}_{bin} \approx 0$ to $\text{FWHM}_{bin} = 0.15\Delta\omega_{in}$ and for three different normalizations of the JSA. These normalizations correspond to different pump strengths of the PDC process and are chosen to represent JSAs with mean photon numbers of 1, 5, and 10. The results are depicted in Fig. 5.

One can immediately see from Fig. 5 that a minimum in purity can be observed for bins that are smaller than the width of the JSA. This can be explained by strong edge effects during the coherent filtering. Furthermore, no clear optimal regime for operating the LOQN is observable; instead, in the limit of larger bins, both purity and squeezing continuously improve. Note that the continuous improvement of the output state's purity is due to the fact that in the limit of larger bins, the distribution of Schmidt coefficients of the converted part from the JSA becomes

broader. As this broadening occurs, many of the coefficients tend to become roughly equal (commonly referred to as degeneracy). This results in a freedom in basis choice and allows the frequency-bin basis to approach pure states. This result is in contrast to heralded single-photon sources from type-2 PDC, where strong spectral intensity filtering on the herald results in highly pure heralded states [42], and showcases the fundamentally different behavior of a coherent filter.

IV. SCALING

We argue that our scheme is an excellent candidate for the resource-efficient scaling of the fully programmable LOQN to higher numbers of contributing modes, since the complete network can be achieved in only two non-linear waveguides. To understand the fundamental limits and get an estimate of achievable dimensionality of the systems, we perform simulations to investigate how many bins can be implemented within the given spectral window $\Delta\omega_{in}$. For this, we first consider one output frequency bin of an MQPG with N input bins, to evaluate the performance of individual output channels. We use Gaussian bins A_k that are positioned maximally spaced, equally distributed, and symmetrically placed around the degeneracy point. We avoid overlap by keeping the minimal separation above 2FWHM_{bin} of the bins. For the PDC, we consider the JSA from the previous section, with different widths FWHM_{JSA} , all normalized to a mean photon number of 20. To account for different programming of the LOQN, we consider the two extremal cases of equal and alternating phases (0 and π) between neighboring bins. Since, for these cases, SMS states are expected in the output, we evaluate the performance via the purity and squeezing strength. These quantities are depicted in Fig. 6 for varying bin widths and numbers of used bins.

The upper left corner, representing big bins with sufficient separation, is expectedly the only area providing good purity and squeezing values for both cases. Therefore, the LOQN can operate only in this specific region. However, it also becomes apparent that, for thinner JSAs, the usable area becomes larger and more homogeneous, thereby demonstrating that the dimensionality of the LOQN reachable with our approach goes well beyond the two modes of the frequency-bin beam splitter.

To also investigate how these imperfections influence the implementation of full $N \times N$ interferometers, we simulate such systems using our model. For this, we use a JSA with $\text{FWHM}_{JSA} = 0.02\Delta\omega_{in}$ and implement MQPGs with varying input bin widths FWHM_{bin} and dimensionalities N . The input bins are again placed symmetrically around the degeneracy point and are spaced sufficiently far apart to avoid overlaps. Since we assume a perfect mapping of the MQPG, we can characterize the output state by simulating the $2N \times 2N$ covariance matrix σ of the N output modes.

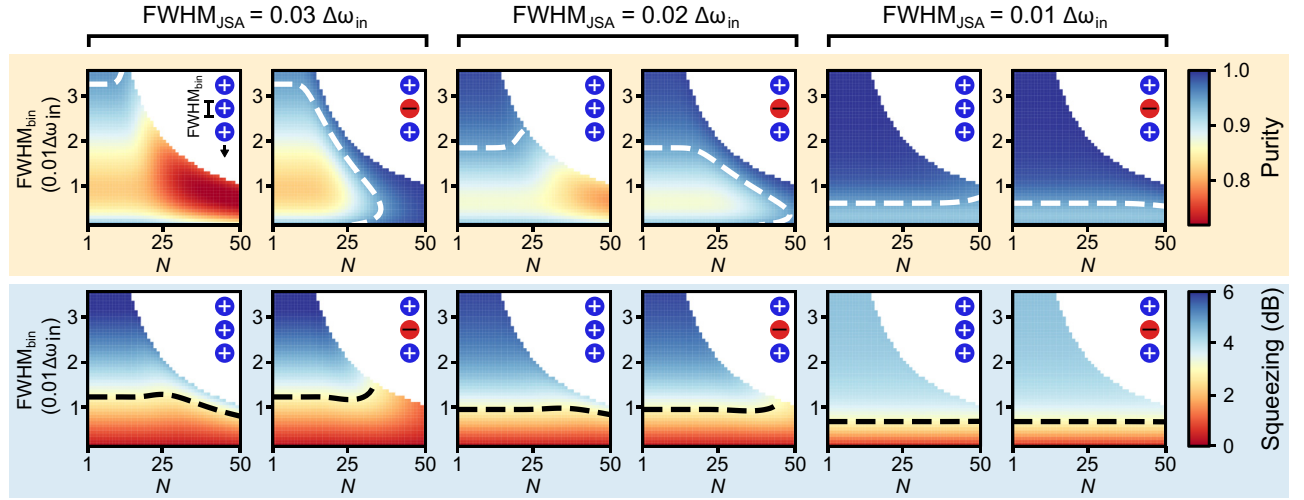


FIG. 6. Investigation of squeezing a purity of the single-mode squeezed state in the output channel of an MQPG after filtering from a type-0 PDC state, for varying frequency bin widths and numbers of used bins. The white area is inaccessible, because neighboring bins overlap. We investigate the cases of equal and alternating (0 and π) phases. Top: purity. Bottom: squeezing in the output channel. Three different JSAs are considered with $\text{FWHM}_{\text{JSA}} = 0.03\Delta\omega_{\text{in}}, 0.02\Delta\omega_{\text{in}}, 0.01\Delta\omega_{\text{in}}$. The dashed white line corresponds to a threshold purity of $\gamma_0 = 0.95$ and the black dashed lines correspond to a squeezing value of $S_0 = 3$ dB.

We compare the result with a perfect LOQN (pure input squeezed states), which is evaluated using the simulation toolbox STRAWBERRY FIELDS [47]. For the squeezed inputs of the ideal LOQN, the squeezing parameter α was chosen to match the squeezing level of the coherently filtered states in the input bins of the MQPG. We perform this simulations for different random interferometer configurations (given by U) and compare the results by calculating the fidelity $F = \text{tr}[\sqrt{\rho_A \rho_B} \sqrt{\rho_A}] = [\det(\sigma_A + \sigma_B)]^{-1/4}$ [48]. The results are depicted in Fig. 7 together with the purity of the system. The resulting fidelity indicates that our scheme is capable of implementing full LOQNs. However, we also find that the purity and fidelity decrease for larger N . Since this decrease results from the accumulation of the imperfection of the individual channels, the overall performance of the LOQN can again be improved by using larger input bins (see Fig. 7).

We also want to highlight that the investigated widths of the JSAs are well achievable with state-of-the-art LiNbO₃ waveguides. The thinnest JSA with $\text{FWHM}_{\text{JSA}} = 0.01\Delta\omega_{\text{in}}$, for example, well approximates the JSA achievable in a 4-cm-long waveguide on an input window $\Delta\omega_{\text{in}}$ corresponding to 50 nm centered at 1550 nm. Note that, due to the parallel alignment of the phase-matching and pump functions of the type-0 source, it is also possible to reduce the width of the JSA by simply reducing the width of the pump spectrum.

In Appendix B we display a rough estimate of the accessible dimensionalities of our scheme. We find that, with state-of-the-art MQPGs, input numbers in the hundreds could be expected. One limitation of our scheme is the realization of large numbers of output modes, owing to

the fact that the different outputs have to share the same pump bandwidth. However, it is possible to cascade multiple MQPGs, since all superposition modes that are not addressed pass the device unconverted. These modes can

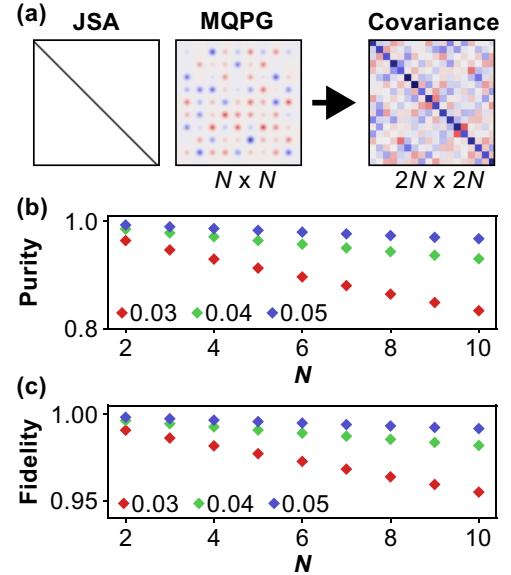


FIG. 7. Simulation of the full $N \times N$ frequency-bin interferometer. (a) Schematic of the simulations. The covariance matrix at the output of the MQPG is calculated. (b) The purity evaluated from the covariance matrix for different MQPGs. The colors label different input bin widths $\text{FWHM}_{\text{bin}} = 0.03\Delta\omega_{\text{in}}, 0.04\Delta\omega_{\text{in}}, 0.05\Delta\omega_{\text{in}}$. (c) The fidelity between the output state of the MQPG and the state after an ideal LOQN (both are implementing the same interferometer).

therefore be accessed by a consecutive MQPG corresponding to different outputs, albeit at the cost of increasing the number of required waveguides needed for implementation.

V. DISCUSSION

The scheme presented in this work considers frequency bins as a basis for the LOQN, since these are relatively easy to shape and control. But, in principle, the scheme can be implemented in many other TM bases, e.g., Hermite-Gaussian modes. For these, we have found similar results, with the difference that, for centered HG modes, the input states of the LOQN are SMS instead of TMS. Furthermore, we want to highlight again that our scheme does not assume any specific detection method and even the use of different detection methods in different output channels can be imagined. Our scheme does not require any phase stability between PDC and the MQPG, unless one wishes to interfere the output of the MQPG with an independent optical field (e.g., for detection in the photon-number basis). This is because both nonlinear processes are intrinsically phase stable, and a relative phase between them only results in an unknown global phase of the output modes. In this case two repetition-rate-locked pump laser sources for PDC and the MQPG are sufficient for an implementation of the LOQN.

Moreover, we want to mention that we assume perfect MQPGs (unity conversion efficiency and perfect mapping of modes) throughout this work, because we want to focus on the fundamental limits of the presented scheme. However, our theoretical framework also allows us to study more complicated scenarios, including imperfections, since it only considers a general TF and JSA as input. This, for example, allows us to include multimode effects in the outputs of the MQPG, which can occur for imperfect PM functions. In this case one output of the MQPG is described by a bigger covariance matrix, which describes all modes contributing to said output.

VI. CONCLUSION

In this work we have presented a novel scheme for the implementation of LOQNs based on frequency conversion, which utilizes so-called multioutput quantum pulse gates. This approach allows one to construct a fully programmable and inherently phase-stable multiport interferometer on a frequency-bin basis. We demonstrate the feasibility of this approach and its natural compatibility with broadband squeezing sources, by performing simulations based on a detailed theoretical model in the continuous-variable picture.

A potential experimental implementation of LOQNs based on this approach requires only two nonlinear waveguides for the highly multimode input state generation and the programmable interferometer. In contrast to other

encodings (e.g., spatial or temporal domain) the achievable dimensionality of this LOQN is mainly limited by spectral shaping resolution and not by the number of utilized components (e.g., beam splitters). Because of this, the relatively low demand on required components, and the inherent compatibility with integrated optical platforms, we believe that this approach is a promising candidate for scaling up LOQNs toward practical applications. We find that, with state-of-the-art MQPGs, a few hundred input modes are feasible. However, reducing the phase-matching width of MQPGs, by for example utilizing resonators, could allow for much larger networks. We expect our approach to become an enabling platform for future quantum technologies thanks to its inherent scalability, full programmability, and ease of experimental implementation.

Note added. Recently, we became aware of similar work [49].

ACKNOWLEDGMENT

The authors thank J. Sperling and M. Santandrea for helpful discussions. This work was supported in part by the European Commission H2020- FET-OPEN-RIA (STORMYTUNE), under Grant No. 899587.

APPENDIX A: SIMULATED EXPERIMENT

In the main text we considered idealized systems; however, to demonstrate the feasibility of the proposed systems, here we provide simulations of realistically achievable nonlinear processes. These simulations are based on the Sellmeier equations of titanium in-diffused LiNbO₃ waveguides. In the left panel of Fig. 8 the joint spectral amplitude of a 1-cm-long waveguide, pumped with a 3-ps-long pulsed laser at 775 nm, is depicted. To achieve degeneracy at 1550 nm, a poling period of

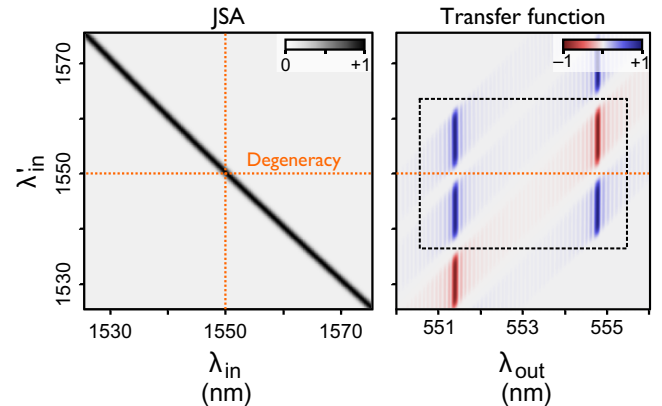


FIG. 8. Simulations of the joint spectral amplitude from a type-0 PDC process in the LiNbO₃ waveguide (left) and the transfer function of a two-output MQPG implementing a frequency beam splitter (right; represented by the dotted box).

16.93 μm is considered. Note that no sinc side lobes are visible, since the pump width of 0.3 nm is narrower than the phase matching. For the simulation of the transfer function of a two-output MQPG [depicted in right panel of Fig. 8], we consider a poling period of 4.33 μm , a 1-cm-long waveguide, and the superstructure presented in Ref. [50]. To simulate a frequency-bin beam splitter as discussed in the main text, we consider a pump that is composed of four 3-nm-wide bins. The bins are centered around a central wavelength of 860 nm and could, for example, be carved out from a 100-fs-long pulse. Note that these simulations utilize conservative assumptions for the design parameters, e.g., MQPG waveguides with length around 7 cm are obtainable.

APPENDIX B: SCALABILITY OF THE APPROACH

Here we estimate the scalability of our approach to higher dimensions. We measure this dimensionality in terms of the number of achievable input bins N_{in} . This number is fundamentally limited by four factors. (1) The spectral range $\Delta\omega_{\text{in}}$ over which the type-0 PDC can provide TMS states between the frequency bins. (2) The pump bandwidth $\Delta\omega_{\text{pump}}$ of the MQPG that also limits the available input range. This bandwidth also has to be divided by the number of output bins N_{out} , since each output requires an equally broad pump region. (3) The phase-matching width δ_{MQPG} of the MQPG because the MQPG is working under the assumption that the PM is narrower than the pump structure (bins). (4) The PM or pump width δ_{PDC} of the PDC, since the LOQN's operation is limited by this number, as discussed in the main text. The first two points limit the available input range, while the latter two limit the minimal bin size; therefore, we estimate the amount of available input bins by

$$N_{\text{in}} = \frac{\text{available input range}}{\text{minimal bin size}} = \frac{\min(\Delta\omega_{\text{in}}, \Delta\omega_{\text{pump}}/N_{\text{out}})}{\max(\delta_{\text{PDC}}, \delta_{\text{MQPG}})}. \quad (\text{B1})$$

The results of this estimation are depicted in Fig. 9, together with the limits set by experimentally demonstrated MQPGs [24,51]. Considering a 7-cm-long MQPG together with a 4-THz pump spectrum for example could allow for a system with 200 input bins but only one output. However, we can also observe that this number reduces quickly for a higher number of outputs according to $1/N_{\text{out}}$. Since the number of available pump bins is given by $N_{\text{pump}} = N_{\text{in}}(N_{\text{out}} = 1)$, we can estimate the achievable dimensionality of a full $N \times N$ interferometer by $\sqrt{N_{\text{pump}}}$, which in the given example would result in a (14×14) -dimensional system. Note that it is also possible to obtain

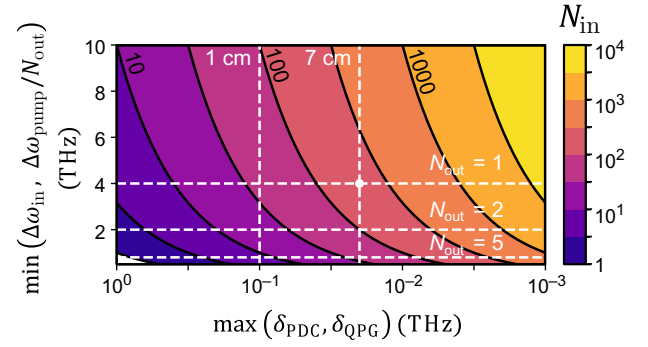


FIG. 9. Estimation of the achievable number of input bins for different parameters of the available bandwidth of the network (vertical axis) and for different phase-matching widths (horizontal axis). The horizontal white lines correspond to an MQPG with a pump bandwidth of 4 THz and different numbers of outputs. The vertical lines correspond to MQPGs with different lengths.

a larger $N \times N$ interferometer for the same limits by sacrificing levels of programmability, by using one pump bin to intersect multiple PM peaks.

APPENDIX C: THEORY OF TYPE-0 PDC

Type-0 PDC in a single spatial mode and polarization (e.g., in waveguides) can, in the low-gain regime (neglecting time ordering), be described by the unitary operator [37]

$$\hat{U}_{\text{PDC}} = \exp \left(-\frac{i}{\hbar} \int d\omega_i d\omega'_i f(\omega_i, \omega'_i) \times \hat{b}^\dagger(\omega_i) \hat{b}^\dagger(\omega'_i) + \text{H.c.} \right). \quad (\text{C1})$$

Here, $f(\omega_i, \omega'_i)$ is the JSA of the process. In type-0 PDC the signal and idler are indistinguishable and therefore the JSA has to fulfill $f(\omega_i, \omega'_i) = f(\omega'_i, \omega_i)$. A common approach in describing PDC states is by performing a Schmidt decomposition of the JSA

$$-\frac{i}{\hbar} f(\omega_i, \omega'_i) = \sum_k r_k^P \phi_k^{P*}(\omega_i) \phi_k^{P*}(\omega'_i), \quad (\text{C2})$$

which results in a set of orthogonal Schmidt modes $\{\phi_k^P(\omega_i)\}$ with Schmidt coefficients r_k^P [52]. These modes are equal for the signal and idler because they are indistinguishable. By defining the operators $\hat{\phi}_k^\dagger := \int d\omega_i \phi_k^{P*}(\omega_i) \hat{b}^\dagger(\omega_i)$, the Schmidt decomposition allows us to rewrite unitary (C1) as

$$\hat{U}_{\text{PDC}} = \bigotimes_k \exp[r_k^P (\hat{\phi}_k^\dagger)^2 + \text{H.c.}] = \bigotimes_k \hat{S}_k^{(\text{SMS})}(r_k^P), \quad (\text{C3})$$

which corresponds to multiple independent single-mode squeezing operators on the different Schmidt modes. However, besides this fundamental structure of type-0 PDC sources, we show in the main text that in the case of highly multimode PDC, two-mode squeezed states can also be extracted from such a source.

In the Heisenberg picture, the PDC process is described by the linear Bogoliubov transformation [29,53]

$$\begin{aligned}\hat{b}'(\omega_i) &= \int d\omega'_i U^P(\omega_i, \omega'_i) \hat{b}(\omega'_i) \\ &+ \int d\omega'_i V^P(\omega_i, \omega'_i) \hat{b}^\dagger(\omega'_i).\end{aligned}\quad (\text{C4})$$

Here, U^P and V^P can be expressed with help of the Schmidt modes $\phi_k^P(\omega_i)$ and can therefore be directly obtained from the JSA. They have the form [29]

$$\begin{aligned}U^P(\omega_i, \omega'_i) &= \sum_k \phi_k^{P*}(\omega_i) \cosh(r_k^P) \phi_k^P(\omega'_i), \\ V^P(\omega_i, \omega'_i) &= \sum_k \phi_k^{P*}(\omega_i) \sinh(r_k^P) \phi_k^{P*}(\omega'_i).\end{aligned}\quad (\text{C5})$$

This procedure of determining the U^P and V^P matrices from the JSA via Eq. (C5), as used in the main text, is however only possible when time-ordering effects are neglected [29]. To include these effects, it is necessary to solve the nonlinear propagation equation

$$\begin{aligned}\partial_z \hat{b}(\omega; z) &= ik(\omega) \hat{b}(\omega; z) \\ &+ \frac{1}{L_{\text{NL}}} \int d\omega' P(\omega' + \omega; z) \hat{b}^\dagger(\omega'; z),\end{aligned}\quad (\text{C6})$$

by integrating over length L of the nonlinear medium [53,54] to obtain U^P and V^P . The first term in Eq. (C6) contains the dispersion properties in $k(\omega)$ and describes the free propagation. The second term describes the nonlinear interaction. Here, P is the complex spectrum of the pump pulse, which is normalized via $\int d\omega |P(\omega)| = 1$, and L_{NL} determines the strength of the nonlinear interaction. We use Eq. (C6) in Appendix F to validate our results from the main text.

APPENDIX D: THEORY OF SFG

Because the multioutput quantum pulse gate is based on an SFG process, it can be described by the unitary operator of a general SFG process [29]

$$\begin{aligned}\hat{U}_{\text{SFG}} &= \exp \left(-\frac{i}{\hbar} \int d\omega_i d\omega_o G(\omega_i, \omega_o) \right. \\ &\quad \times \hat{a}^\dagger(\omega_o) \hat{b}(\omega_i) + \text{H.c.} \left. \right).\end{aligned}\quad (\text{D1})$$

Here, $G(\omega_i, \omega_o)$ is the TF of the process, which describes how the input frequencies ω_i are converted to the output frequencies ω_o . We again neglect time-ordering effects [29]. Note that we choose one of the input fields of the MQPG to be represented by the same operators $\hat{b}(\omega_i)$ as the field of the PDC process.

In the Heisenberg picture the SFG process takes the form of the Bogoliubov transformations [29]

$$\begin{aligned}\hat{b}''(\omega_i) &= \int d\omega'_i U_b^Q(\omega_i, \omega'_i) \hat{b}'(\omega'_i) \\ &+ \int d\omega'_o V_b^Q(\omega_i, \omega'_o) \hat{a}'(\omega'_o),\end{aligned}\quad (\text{D2a})$$

$$\begin{aligned}\hat{a}''(\omega_o) &= \int d\omega'_o U_a^Q(\omega_o, \omega'_o) \hat{a}'(\omega'_o) \\ &- \int d\omega'_i V_a^Q(\omega_o, \omega'_i) \hat{b}'(\omega'_i).\end{aligned}\quad (\text{D2b})$$

Functions U and V can again be calculated by performing a Schmidt decomposition of the TF that takes the form

$$-\frac{i}{\hbar} G(\omega_i, \omega_o) = -\sum_k r_k^Q \phi_k^Q(\omega_i) \psi_k^{Q*}(\omega_o) \quad (\text{D3})$$

and results in the two orthonormal bases $\{\phi_k^Q(\omega_i)\}$ and $\{\psi_k^Q(\omega_o)\}$. This then allows us to connect the Schmidt modes to the Bogoliubov transformations via [29]

$$U_b^Q(\omega_i, \omega'_i) = \sum_k \phi_k^{Q*}(\omega_i) \cos(r_k^Q) \phi_k^Q(\omega'_i), \quad (\text{D4a})$$

$$V_b^Q(\omega_i, \omega'_o) = \sum_k \phi_k^{Q*}(\omega_i) \sin(r_k^Q) \psi_k^Q(\omega'_o), \quad (\text{D4b})$$

$$U_a^Q(\omega_o, \omega'_o) = \sum_k \psi_k^{Q*}(\omega_o) \cos(r_k^Q) \psi_k^Q(\omega'_o), \quad (\text{D4c})$$

$$V_a^Q(\omega_o, \omega'_i) = \sum_k \psi_k^{Q*}(\omega_o) \sin(r_k^Q) \phi_k^Q(\omega'_i). \quad (\text{D4d})$$

Defining the broadband operators $\hat{R}_k = \int d\omega_o \psi_k^Q(\omega_o) \hat{a}(\omega_o)$ and $\hat{H}_k = \int d\omega_i \phi_k^Q(\omega_i) \hat{b}(\omega_i)$ corresponding to the Schmidt modes allows us to simply transformations (D2) to

$$\hat{H}'_k = \cos(r_k^Q) \hat{H}_k + \sin(r_k^Q) \hat{R}_k, \quad (\text{D5})$$

$$\hat{R}'_k = \cos(r_k^Q) \hat{R}_k - \sin(r_k^Q) \hat{H}_k. \quad (\text{D6})$$

These equations have the same structure as Eqs. (11); however, since we are considering a general SFG, modes (\hat{H}_k

and \hat{R}_k) can spectrally overlap and are therefore not separately detectable via spectral multiplexing. This is one of the features enabled by considering a TF of the form (7), realizable in MQPGs, which converts to well-separated output modes O_k . In other words, the Schmidt modes of the MQPG with TF (7) are the superposition modes S_k and the output modes O_k , with degenerate (equal-weight) Schmidt coefficients. If time-ordering effects cannot be neglected, the U and V matrices can be obtained via more involved simulations [55]. However, it was demonstrated that time-ordering effects in QPGs can be mitigated by combining two QPGs in an interferometric scheme [34].

APPENDIX E: COMBINING PDC AND THE MQPG

The objective of our model is to describe the output quantum state of the MQPG. Since each output channel corresponds to one mode O_k , this output state can be characterized in terms of the density matrix σ on the basis of the output modes O_k [see Eq. (19)]. We describe the dynamics of the two nonlinear processes in the Heisenberg picture by consecutively applying Eqs. (17) and (10) to the output operators

$$\hat{O}_k'' = \int d\omega_o O_k(\omega_o) \hat{a}''(\omega_o) \quad (\text{E1})$$

and obtain

$$\begin{aligned} \hat{O}_k'' &= \int d\omega_o H_k^1(\omega_o) \hat{a}'(\omega_o) + \int d\omega_i H_k^2(\omega_i) \hat{b}(\omega_i) \\ &\quad + H_k^3(\omega_i) \hat{b}^\dagger(\omega_i), \end{aligned} \quad (\text{E2})$$

where we have defined the functions

$$H_k^1(\omega_o) = \int d\omega'_o O_k(\omega'_o) U_a^Q(\omega'_o, \omega_o), \quad (\text{E3a})$$

$$H_k^2(\omega_i) = - \int d\omega'_o d\omega'_i O_k(\omega'_o) V_a^Q(\omega'_o, \omega'_i) V^P(\omega'_i, \omega_i), \quad (\text{E3b})$$

$$H_k^3(\omega_i) = - \int d\omega'_o d\omega'_i O_k(\omega'_o) V_a^Q(\omega'_o, \omega'_i) V^P(\omega'_i, \omega_i). \quad (\text{E3c})$$

These functions can be derived from a given JSA and TF by utilizing Eqs. (C5) and (D4). To now describe the output state of the MQPG, we first observe that we can neglect displacement [second term of Eq. (19)], since we assume vacuum states in front of the nonlinear elements and do not consider seeding. By considering the operator order of Eq. (18), the covariance matrix can be constructed from the

2×2 submatrices

$$\tilde{\sigma}_{kl} = \begin{pmatrix} \langle \hat{X}_k \hat{X}_l \rangle + \langle \hat{X}_l \hat{X}_k \rangle & \langle \hat{X}_k \hat{Y}_l \rangle + \langle \hat{Y}_l \hat{X}_k \rangle \\ \langle \hat{Y}_k \hat{X}_l \rangle + \langle \hat{X}_l \hat{Y}_k \rangle & \langle \hat{Y}_k \hat{Y}_l \rangle + \langle \hat{Y}_l \hat{Y}_k \rangle \end{pmatrix}, \quad (\text{E4})$$

where k and l label two modes from $\{\hat{O}_k\}$. The submatrices for $k = l$ describe the substates in the individual channels and, for $k \neq l$, it describes the quadrature covariances between two different output modes. To calculate these submatrices, we first express the individual elements in terms of the output operators and obtain

$$\langle \hat{X}_k \hat{X}_l \rangle = \frac{1}{2} \langle \hat{O}_k \hat{O}_l + \hat{O}_k \hat{O}_l^\dagger + \hat{O}_k^\dagger \hat{O}_l + \hat{O}_k^\dagger \hat{O}_l^\dagger \rangle, \quad (\text{E5a})$$

$$\langle \hat{X}_k \hat{Y}_l \rangle = \frac{1}{2i} \langle \hat{O}_k \hat{O}_l - \hat{O}_k \hat{O}_l^\dagger + \hat{O}_k^\dagger \hat{O}_l - \hat{O}_k^\dagger \hat{O}_l^\dagger \rangle, \quad (\text{E5b})$$

$$\langle \hat{Y}_k \hat{X}_l \rangle = \frac{1}{2i} \langle \hat{O}_k \hat{O}_l + \hat{O}_k \hat{O}_l^\dagger - \hat{O}_k^\dagger \hat{O}_l - \hat{O}_k^\dagger \hat{O}_l^\dagger \rangle, \quad (\text{E5c})$$

$$\langle \hat{Y}_k \hat{Y}_l \rangle = \frac{-1}{2} \langle \hat{O}_k \hat{O}_l - \hat{O}_k \hat{O}_l^\dagger - \hat{O}_k^\dagger \hat{O}_l + \hat{O}_k^\dagger \hat{O}_l^\dagger \rangle. \quad (\text{E5d})$$

By assuming vacuum input states and inserting Eqs. (E3), we are then able to calculate the terms in Eqs. (E5), which results in

$$\langle 0 | \hat{O}_k \hat{O}_l | 0 \rangle = \int d\omega_i H_k^2(\omega_i) H_l^3(\omega_i),$$

$$\begin{aligned} \langle 0 | \hat{O}_k \hat{O}_l^\dagger | 0 \rangle &= \int d\omega_o H_k^1(\omega_o) H_l^{1*}(\omega_o) \\ &\quad + \int d\omega_i H_k^2(\omega_i) H_l^{2*}(\omega_i), \end{aligned}$$

$$\langle 0 | \hat{O}_k^\dagger \hat{O}_l | 0 \rangle = \int d\omega_i H_k^{3*}(\omega_i) H_l^3(\omega_i),$$

$$\langle 0 | \hat{O}_k^\dagger \hat{O}_l^\dagger | 0 \rangle = \int d\omega_i H_k^{3*}(\omega_i) H_l^{2*}(\omega_i).$$

This now allows us to calculate the complete covariance matrix at the output of the MQPG. We want to mention that this approach can be applied to describe a general system composed of type-0 PDC and an SFG process, since it only requires a JSA and TF as input. The output modes then take the form of the output Schmidt basis $[\psi_k^Q(\omega_o)]$ of the TF. This, for example, allows us to study multimode effects occurring in imperfect MQPGs.

APPENDIX F: EFFECTS OF HIGH-GAIN TYPE-0 PDC

To investigate the validity of our scheme even under the consideration of time-ordering effects in the type-0 PDC source, we repeat the calculations presented in Fig. 5, but this time use U^P and V^P matrices obtained from solving Eq. (C6). This can be achieved numerically using split-step methods [53,54], but here we adapt the matrix-exponential-based approach presented in Refs. [56–58] for type-2 PDC.

For this, we consider a grid of discretized frequencies ω_n with a separation $\Delta\omega$ and the two column vectors $\mathbf{b}_n(z) := \hat{b}(\omega_n; z)$ and $\mathbf{b}_n^\dagger(z) := \hat{b}^\dagger(\omega_n; z)$. This allows us to rewrite Eq. (C6) (and its complex conjugate) in the matrix form

$$\partial_z \begin{bmatrix} \mathbf{b}(z) \\ \mathbf{b}^\dagger(z) \end{bmatrix} = \underbrace{\begin{bmatrix} \mathbf{K} & \mathbf{P} \\ \mathbf{P}^* & -\mathbf{K} \end{bmatrix}}_{:=\mathbf{M}} \begin{bmatrix} \mathbf{b}(z) \\ \mathbf{b}^\dagger(z) \end{bmatrix} \quad (\text{F1})$$

with

$$\mathbf{K}_{n,m} = i\Delta k(\omega_n)\delta_{nm} \quad \text{and} \quad \mathbf{P}_{n,m} = \frac{\Delta\omega}{L_{\text{NL}}} P(\omega_n + \omega_m). \quad (\text{F2})$$

Note that we consider $\Delta k(\omega)$ in the comoving frame of the pump and enforce phase matching by setting it to 0 at the central frequency. Furthermore, we neglect pump dispersion and depletion to remove the z dependence of P in Eq. (C6), which allows us to solve Eq. (F1) via the matrix exponential

$$\begin{bmatrix} \mathbf{b}(z+L) \\ \mathbf{b}^\dagger(z+L) \end{bmatrix} = e^{\mathbf{M}L} \begin{bmatrix} \mathbf{b}(z) \\ \mathbf{b}^\dagger(z) \end{bmatrix} = \begin{bmatrix} U^P \Delta\omega & V^P \Delta\omega \\ V^{P*} \Delta\omega & U^{P*} \Delta\omega \end{bmatrix} \begin{bmatrix} \mathbf{b}(z) \\ \mathbf{b}^\dagger(z) \end{bmatrix}. \quad (\text{F3})$$

Comparing Eq. (F3) to the Bogoliubov transformation (17), it becomes clear that functions U^P and V^P can be directly obtained as submatrices of the matrix exponential.

We perform these simulations for type-0 PDC in a 1-cm-long LiNbO₃ waveguide pumped with 3-ps-long pulses at 775 nm, which in a 50-nm window approximates the JSA used in Fig. 5. Inserting the resulting U^P and V^P matrices for different coupling strengths L_{NL} into our simulation framework, we obtain the results depicted in Fig. 10. One can see that in the low-gain regime, the time-ordering effects do not result in a deviation from our model presented in Fig. 5, which verifies the assumptions made in the presented regimen. However, when going to higher squeezing levels (roughly 15 dB), the purity does not converge toward 1 anymore and reaches a maximal value. This agrees with the findings in Ref. [40] where it is predicted that time-ordering effects in type-0 PDC should not be significant below 12 dB.

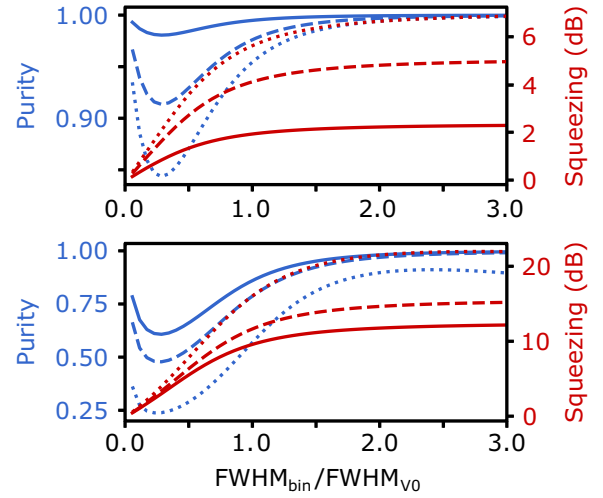


FIG. 10. Squeezing and purity calculated from the covariance matrix after the frequency beam splitter for different relative input bin widths $\text{FWHM}_{\text{bin}}/\text{FWHM}_{V_0}$, where FWHM_{V_0} is the width of V^P in the low-gain limit. The different line types correspond to different pump strengths in the PDC process, which is simulated including time-ordering effects. Top: low-gain regime with $L_{\text{NL}} = L/0.3$ (solid), $L/0.65$ (dashed), $L/0.9$ (dotted). Bottom: high-gain regime with $L_{\text{NL}} = L/1.6$ (solid), $L/2.0$ (dashed), $L/3.0$ (dotted).

- [1] S. Aaronson and A. Arkhipov, The computational complexity of linear optics, *Theory Comput.* **9**, 143 (2013).
- [2] C. S. Hamilton, R. Kruse, L. Sansoni, S. Barkhofen, C. Silberhorn, and I. Jex, Gaussian boson sampling, *Phys. Rev. Lett.* **119**, 170501 (2017).
- [3] R. Kruse, C. S. Hamilton, L. Sansoni, S. Barkhofen, C. Silberhorn, and I. Jex, Detailed study of Gaussian boson sampling, *Phys. Rev. A* **100**, 032326 (2019).
- [4] N. C. Menicucci, P. van Loock, M. Gu, C. Weedbrook, T. C. Ralph, and M. A. Nielsen, Universal quantum computation with continuous-variable cluster states, *Phys. Rev. Lett.* **97**, 110501 (2006).
- [5] M. Gu, C. Weedbrook, N. C. Menicucci, T. C. Ralph, and P. van Loock, Quantum computing with continuous-variable clusters, *Phys. Rev. A* **79**, 062318 (2009).
- [6] P. van Loock and S. L. Braunstein, Multipartite entanglement for continuous variables: A quantum teleportation network, *Phys. Rev. Lett.* **84**, 3482 (2000).
- [7] H. Yonezawa, T. Aoki, and A. Furusawa, Demonstration of a quantum teleportation network for continuous variables, *Nature* **431**, 430 (2004).
- [8] A. M. Childs, Universal computation by quantum walk, *Phys. Rev. Lett.* **102**, 180501 (2009).
- [9] S. E. Venegas-Andraca, Quantum walks: A comprehensive review, *Quantum Inf. Process.* **11**, 1015 (2012).
- [10] A. Schreiber, K. N. Cassemiro, V. Potoček, A. Gábris, P. J. Mosley, E. Andersson, I. Jex, and C. Silberhorn, Photons walking the line: A quantum walk with adjustable coin operations, *Phys. Rev. Lett.* **104**, 050502 (2010).

- [11] J. Huh, G. G. Guerreschi, B. Peropadre, J. R. McClean, and A. Aspuru-Guzik, Boson sampling for molecular vibronic spectra, *Nat. Photonics* **9**, 615 (2015).
- [12] L. Bianchi, M. Fingerhuth, T. Babej, C. Ing, and J. M. Arrazola, Molecular docking with Gaussian boson sampling, *Sci. Adv.* **6**, eaax1950 (2020).
- [13] H.-S. Zhong, *et al.*, Quantum computational advantage using photons, *Science* **370**, 1460 (2020).
- [14] L. S. Madsen, F. Laudenbach, M. F. Askarani, F. Rortais, T. Vincent, J. F. F. Bulmer, F. M. Miatto, L. Neuhaus, L. G. Helt, M. J. Collins, A. E. Lita, T. Gerrits, S. W. Nam, V. D. Vaidya, M. Menotti, I. Dhand, Z. Vernon, N. Quesada, and J. Lavoie, Quantum computational advantage with a programmable photonic processor, *Nature* **606**, 75 (2022).
- [15] H.-H. Lu, J. M. Lukens, N. A. Peters, B. P. Williams, A. M. Weiner, and P. Lougovski, Quantum interference and correlation control of frequency-bin qubits, *Optica* **5**, 1455 (2018).
- [16] H.-H. Lu, J. M. Lukens, N. A. Peters, O. D. Odele, D. E. Leaird, A. M. Weiner, and P. Lougovski, Electro-optic frequency beam splitters and tritters for high-fidelity photonic quantum information processing, *Phys. Rev. Lett.* **120**, 030502 (2018).
- [17] H.-H. Lu, E. M. Simmerman, P. Lougovski, A. M. Weiner, and J. M. Lukens, Fully arbitrary control of frequency-bin qubits, *Phys. Rev. Lett.* **125**, 120503 (2020).
- [18] M. Kues, C. Reimer, J. M. Lukens, W. J. Munro, A. M. Weiner, D. J. Moss, and R. Morandotti, Quantum optical microcombs, *Nat. Photonics* **13**, 170 (2019).
- [19] M. Kues, C. Reimer, P. Roztock, L. R. Cortés, S. Sciara, B. Wetzel, Y. Zhang, A. Cino, S. T. Chu, B. E. Little, D. J. Moss, L. Caspani, J. Azaña, and R. Morandotti, On-chip generation of high-dimensional entangled quantum states and their coherent control, *Nature* **546**, 622 (2017).
- [20] H.-H. Lu, M. Liscidini, A. L. Gaeta, A. M. Weiner, and J. M. Lukens, Frequency-bin photonic quantum information, *Optica* **10**, 1655 (2023).
- [21] J. Roslund, R. M. de Araújo, S. Jiang, C. Fabre, and N. Treps, Wavelength-multiplexed quantum networks with ultrafast frequency combs, *Nat. Photonics* **8**, 109 (2014).
- [22] Y. Cai, J. Roslund, G. Ferrini, F. Arzani, X. Xu, C. Fabre, and N. Treps, Multimode entanglement in reconfigurable graph states using optical frequency combs, *Nat. Commun.* **8**, 15645 (2017).
- [23] Y. Cai, J. Roslund, V. Thiel, C. Fabre, and N. Treps, Quantum enhanced measurement of an optical frequency comb, *npj Quantum Inf.* **7**, 82 (2021).
- [24] L. Serino, J. Gil-Lopez, M. Stefszky, R. Ricken, C. Eigner, B. Brecht, and C. Silberhorn, Realization of a multi-output quantum pulse gate for decoding high-dimensional temporal modes of single-photon states, *PRX Quantum* **4**, 020306 (2023).
- [25] S. De, V. Ansari, J. Sperling, S. Barkhofen, B. Brecht, and C. Silberhorn, Realization of high-fidelity unitary operations on up to 64 frequency bins, *Phys. Rev. Res.* **6**, L022040 (2024).
- [26] B. Brecht, D. V. Reddy, C. Silberhorn, and M. Raymer, Photon temporal modes: A complete framework for quantum information science, *Phys. Rev. X* **5**, 041017 (2015).
- [27] C. Fabre and N. Treps, Modes and states in quantum optics, *Rev. Mod. Phys.* **92**, 035005 (2020).
- [28] B. Brecht, A. Eckstein, R. Ricken, V. Quiring, H. Suche, L. Sansoni, and C. Silberhorn, Demonstration of coherent time-frequency Schmidt mode selection using dispersion-engineered frequency conversion, *Phys. Rev. A* **90**, 030302 (2014).
- [29] A. Christ, B. Brecht, W. Maurer, and C. Silberhorn, Theory of quantum frequency conversion and type-II parametric down-conversion in the high-gain regime, *New J. Phys.* **15**, 053038 (2013).
- [30] A. Eckstein, B. Brecht, and C. Silberhorn, A quantum pulse gate based on spectrally engineered sum frequency generation, *Opt. Express* **19**, 13770 (2011).
- [31] Here, for the momentum mismatch in the reference frame of the pump, we assume that $\Delta k(\omega_{\text{in}}, \omega_{\text{out}}) = (1/v_{\text{out}} - 1/v_{\text{pump}})\omega_{\text{out}} - (1/v_{\text{in}} - 1/v_{\text{pump}})\omega_{\text{in}} = (1/v_{\text{out}} - 1/v_{\text{pump}})\omega_{\text{out}}$, since we assume that $v_{\text{pump}} = v_{\text{in}}$ for the group velocities. Therefore, we can write the PM function $\Phi(\Delta k)$ only in dependency of ω_{out} [59].
- [32] This assumption ensures a single-mode character of the conversion process eliminating frequency correlations [59].
- [33] N. Quesada and J. E. Sipe, Effects of time ordering in quantum nonlinear optics, *Phys. Rev. A* **90**, 063840 (2014).
- [34] D. V. Reddy and M. G. Raymer, High-selectivity quantum pulse gating of photonic temporal modes using all-optical Ramsey interferometry, *Optica* **5**, 423 (2018).
- [35] Z. Ma, J.-Y. Chen, M. Garikapati, Z. Li, C. Tang, Y. M. Sua, and Y.-P. Huang, Highly efficient and pure few-photon source on chip, *Phys. Rev. Appl.* **20**, 044033 (2023).
- [36] T. Kouadou, F. Sansavini, M. Ansquer, J. Henaff, N. Treps, and V. Parigi, Spectrally shaped and pulse-by-pulse multiplexed multimode squeezed states of light, *APL Photonics* **8**, 086113 (2023).
- [37] A. Christ, K. Laiho, A. Eckstein, K. N. Cassemiro, and C. Silberhorn, Probing multimode squeezing with correlation functions, *New J. Phys.* **13**, 033027 (2011).
- [38] V. Roman-Rodriguez, B. Brecht, S. K., C. Silberhorn, N. Treps, E. Diamanti, and V. Parigi, Continuous variable multimode quantum states via symmetric group velocity matching, *New J. Phys.* **23**, 043012 (2021).
- [39] C. Weedbrook, S. Pirandola, R. García-Patrón, N. J. Cerf, T. C. Ralph, J. H. Shapiro, and S. Lloyd, Gaussian quantum information, *Rev. Mod. Phys.* **84**, 621 (2012).
- [40] T. Lipfert, D. B. Horoshko, G. Patera, and M. I. Kolobov, Bloch-Messiah decomposition and Magnus expansion for parametric down-conversion with monochromatic pump, *Phys. Rev. A* **98**, 013815 (2018).
- [41] D. B. Horoshko, L. La Volpe, F. Arzani, N. Treps, C. Fabre, and M. I. Kolobov, Bloch-Messiah reduction for twin beams of light, *Phys. Rev. A* **100**, 013837 (2019).
- [42] A. Christ, C. Lupo, M. Reichelt, T. Meier, and C. Silberhorn, Theory of filtered type-II parametric down-conversion in the continuous-variable domain: Quantifying the impacts of filtering, *Phys. Rev. A* **90**, 023823 (2014).
- [43] A. Ferraro, S. Olivares, and M. G. A. Paris, *Gaussian States in Quantum Information* (Bibliopolis, 2005).
- [44] S. L. Braunstein and P. van Loock, Quantum information with continuous variables, *Rev. Mod. Phys.* **77**, 65 (2005).

- [45] E. Fitzke, F. Niederschuh, and T. Walther, Simulating the photon statistics of multimode Gaussian states by automatic differentiation of generating functions, *APL Photonics* **8**, 026106 (2023).
- [46] R. Simon, N. Mukunda, and B. Dutta, A limit formula for the quantum fidelity, *Phys. Rev. A* **49**, 1567 (1994).
- [47] N. Killoran, J. Izaac, N. Quesada, V. Bergholm, M. Amy, and C. Weedbrook, Strawberry fields: A software platform for photonic quantum computing, *Quantum* **3**, 129 (2019).
- [48] G. Spedalieri, C. Weedbrook, and S. Pirandola, A limit formula for the quantum fidelity, *J. Phys. A: Math. Theor.* **46**, 025304 (2013).
- [49] F. Presutti, L. G. Wright, S.-Y. Ma, T. Wang, B. K. Malia, T. Onodera, and P. L. McMahon, Highly multimode visible squeezed light with programmable spectral correlations through broadband up-conversion, *ArXiv:2401.06119*.
- [50] M. H. Chou, K. R. Parameswaran, M. M. Fejer, and I. Brener, Multiple-channel wavelength conversion by use of engineered quasi-phase-matching structures in LiNbO₃ waveguides, *Opt. Lett.* **24**, 1157 (1999).
- [51] J. Gil-Lopez, M. Santandrea, G. Roeland, B. Brecht, C. Eigner, R. Ricken, V. Quiring, and C. Silberhorn, Improved non-linear devices for quantum applications, *New J. Phys.* **23**, 063082 (2021).
- [52] C. K. Law, I. A. Walmsley, and J. H. Eberly, Continuous frequency entanglement: Effective finite Hilbert space and entropy control, *Phys. Rev. Lett.* **84**, 5304 (2000).
- [53] W. Wasilewski, A. I. Lvovsky, K. Banaszek, and C. Radzewicz, Pulsed squeezed light: Simultaneous squeezing of multiple modes, *Phys. Rev. A* **73**, 063819 (2006).
- [54] A. I. Lvovsky, W. Wasilewski, and K. Banaszek, Decomposing a pulsed optical parametric amplifier into independent squeezers, *J. Mod. Opt.* **54**, 721 (2007).
- [55] D. V. Reddy, M. G. Raymer, C. J. McKinstrie, L. Mejling, and K. Rottwitt, Temporal mode selectivity by frequency conversion in second-order nonlinear optical waveguides, *Opt. Express* **21**, 13840 (2013).
- [56] N. Quesada, G. Triginer, M. D. Vidrighin, and J. E. Sipe, Theory of high-gain twin-beam generation in waveguides: from Maxwell's equations to efficient simulation, *Phys. Rev. A* **102**, 033519 (2020).
- [57] M. Houde and N. Quesada, Waveguided sources of consistent, single-temporal-mode squeezed light: The good, the bad, and the ugly, *AVS Quantum Sci.* **5**, 011404 (2023).
- [58] M. Houde and N. Quesada, Perfect pulsed inline twin-beam squeezers, *AVS Quantum Sci.* **6**, 021402 (2024).
- [59] V. Ansari, J. M. Donohue, B. Brecht, and C. Silberhorn, Tailoring nonlinear processes for quantum optics with pulsed temporal-mode encodings, *Optica* **5**, 534 (2018).